Journal of Medicinal Chemistry

pubs.acs.org/jmc

Article

Pyrazolone-Based Zn(II) Complexes Display Antitumor Effects in Mutant p53-Carrying Cancer Cells

Sonila Xhafa, Corrado Di Nicola, Alessia Tombesi, Riccardo Pettinari, Claudio Pettinari, Francesca Scarpelli, Alessandra Crispini, Massimo La Deda, Angela Candreva, Alessia Garufi, Gabriella D'Orazi, Agustín Galindo, and Fabio Marchetti*

Cite This: *J. Med. Chem.* 2024, 67, 15676–15690

Read Online

ACCESS | Metrics & More | Article Recommendations | Supporting Information

ABSTRACT: The synthesis and characterization of nine Schiff bases of pyrazolone ligands **HL^n** (n = 1−9) and the corresponding zinc(II) complexes **1−9** of composition $[Zn(L^n)_2]$ (n = 1−9) are reported. The molecular structures of complexes **2**, **3**, **4**, **8**, and **9** were determined by single-crystal X-ray diffraction analysis, highlighting in all cases a distorted tetrahedral geometry around the Zn(II) ion. Density functional theory studies are performed on both the **HL^n** ligands and the derived complexes. A mechanism of dissociation and hydrolyzation of the coordinated Schiff base ligands is suggested, confirmed experimentally by powder X-ray diffraction study and photophysical studies. Complexes **1−9** were investigated in vitro as anticancer agents, along with mutant p53 (mutp53) protein levels in human cancer cell lines carrying R175H and R273H mutp53 proteins. Only those complexes with the highest Zn(II) ion release via dissociation have shown a significant cytotoxic activity with reduction of mutp53 protein levels.

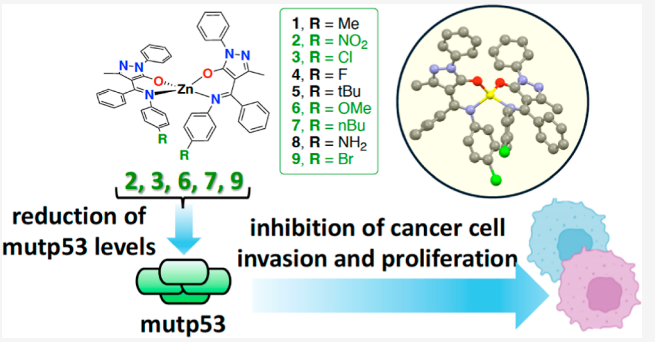

INTRODUCTION

Schiff bases represent an important family of N,O-chelating ligands well-known for thermochromism and photochromism in the solid state also for their biological properties due to the presence of the imine (−N═CH−) group, which is similar to the structures in natural biological system.[1] Among them, pyrazolone-based Schiff bases are attracting growing interest since they have shown interesting biological and pharmacological properties as anti-inflammatory agents, herbicides, bactericides, and fungicides.[2−6] Some examples of these family of ligands and also selected d-block metal complexes with them showed cytotoxicity, anticholinesterase, antioxidant, and enzymes inhibitory activities.[7−10] They are generally prepared by condensation of 4-acyl-5-pyrazolones with substituted amines and can exist in different tautomeric forms (Chart 1).

The zinc(II) coordination chemistry with pyrazolone-based ligands has been investigated in the field of metal-based drugs, showing promising in silico and in vitro antimalarial activity.[11−13]

However, within the field of anticancer Zn-based drugs, these ligands coordinated to Zn(II) ions have been less investigated, despite Zn complexes represent a valuable alternative to platinum (Pt) derivatives, being Zn(II) nontoxic for normal cells compared to other metals and versatile in terms of ligand exchange reactions.[14] Interestingly, Zn(II) complexes have been recognized as Zn suppliers in activating wild-type p53[15] or inhibiting mutant p53 (mutp53), thus reducing tumor progression and improving the cytotoxic activity of chemotherapeutic drugs.[16−25] The p53 oncosuppressor protein is a sequence-specific DNA-binding transcription factor that, in response to stressful stimuli, regulates the transcription of target genes involved in multiple cellular functions including cell cycle arrest, apoptosis, cell growth, DNA repair, cell metabolism, and the immune response.[26] For that reason, tumors cannot stand wild-type p53 that indeed undergoes mutation in 50% of the human cancer and protein deregulation in the other 50%.[27] p53 is a zinc-containing protein that includes one zinc ion as an important cofactor in the DNA-binding domain for transcriptional activity.[28] Interestingly, several mutp53 proteins are prone to the loss of the DBD-bound Zn^{2+} that promotes protein unfolding and aggregation, resulting in loss of wild-type p53 oncosuppressor activity.[29] Changes of p53 conformation, with loss of its tumor suppressor activity, are also achieved by the removal of zinc using for instance chelating agents and can be reversed by

Received: June 7, 2024
Revised: July 29, 2024
Accepted: August 27, 2024
Published: September 2, 2024

Chart 1. Tautomeric forms of 4-aminoalkylidene-5-pyrazolones.

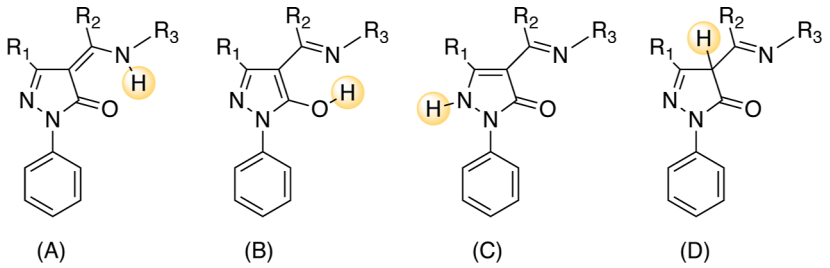

Scheme 1. Synthetic Procedure of Proligands HL^n

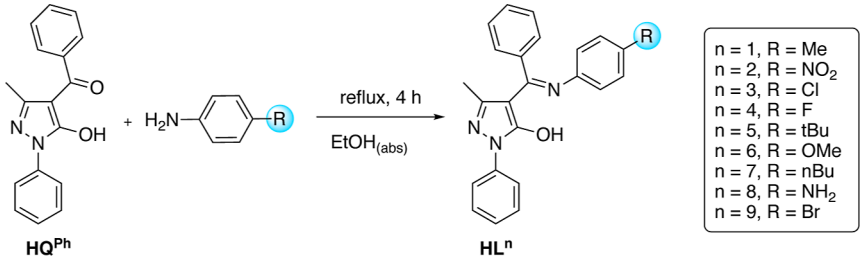

Scheme 2. Synthetic Procedure of Complexes $[Zn(Ln)_2]$ 1−9

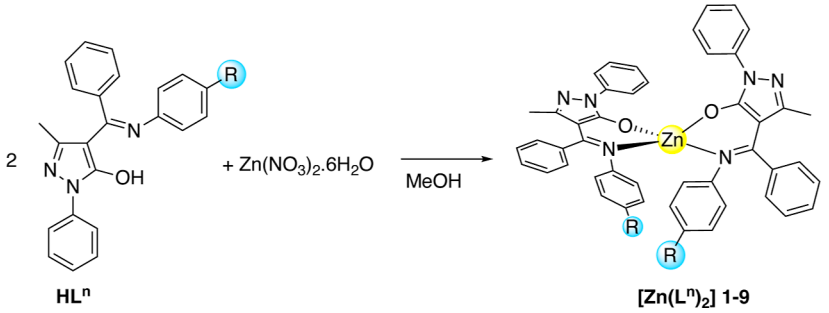

adding zinc.[30] Restoration of wild-type structure and function to mutp53 with small molecules and with zinc complexes is one of the holy grails in cancer therapy as some mutp53 protein may acquire oncogenic activity and promote tumor progression, chemoresistance, and metastasis.[23,31] For those reasons, in this study, we investigated the anticancer effects of the pyrazolone-based Zn(II) complexes in human cells lines carrying two different mutp53 proteins, that is breast cancer SKBR3 (carrying p53R175H mutation), and glioblastoma U373MG (carrying p53R273H mutation) cells,[22] two of the most common p53 mutations[32] that contribute to tumor progression and chemoresistance.[33] The p53 mutations R273H and R175H are classified as contact or structural mutations, respectively,[32] and have been previously shown to benefit of Zn(II) supplementation to restore wild-type p53 activity, reduce mutp53 protein levels, and increase anticancer drugs cytotoxicity leading to tumor regression.[22]

We have investigated recently a number of pyrazolone-based ligands with chelating ability toward arene-Ru(II) acceptors and found that some metal complexes possess cytotoxicity toward a panel of human cancer cells with multi onco-target activity which triggers apoptosis irrespective of the acquired resistance to a DNA-targeting drug such as cisplatin.[34−37] In continuation with our previous studies, herein we present the coordination chemistry of a series of 4-aminoalkylidene-5-pyrazolone molecules, their derived homoleptic Zn(II) complexes, and correlation studies on their structural, photophysical, and bioactivity properties with the different substituents on the aromatic moiety of the pyrazolone-based ligands coordinated to the Zn(II) ion. By investigating their behavior in solution, we verified that these complexes hydrolyze, releasing zinc ions, and the extension of hydrolysis can be correlated with mutp53 downregulation and reduction of cancer cell proliferation and invasiveness. Moreover, a theoretical in-depth analysis with a particular focus on the eventual mechanism of ligand dissociation of the Zn(II) derivatives, in relation to the different substituents on the aromatic moiety of the pyrazolone-based ligands, is presented.

RESULTS AND DISCUSSION

The aminoalkylidene-5-pyrazolones HL^n (n = 1−9) were prepared by reacting 1-phenyl-3-methyl-4-benzoyl-5-pyrazolone with some 4-substituted anilines in absolute ethanol under refluxing conditions, as shown in Scheme 1 below. The Schiff bases and corresponding Zn(II) complexes with R = Me, OMe, F, *t*Bu, NO_2, and NH_2 have been recently reported, and their solid-state luminescence investigated but with limited characterization in solution,[38] whereas those with R = nBu, Cl, and Br are completely new.

They are yellow powder, stable in air at room temperature, and easily soluble in common organic solvents, such as DMSO, DMF, chlorinated solvents, acetone, and acetonitrile but poorly soluble in water, alcohols, and ethers.

https://doi.org/10.1021/acs.jmedchem.4c01298
J. Med. Chem. 2024, 67, 15676−15690

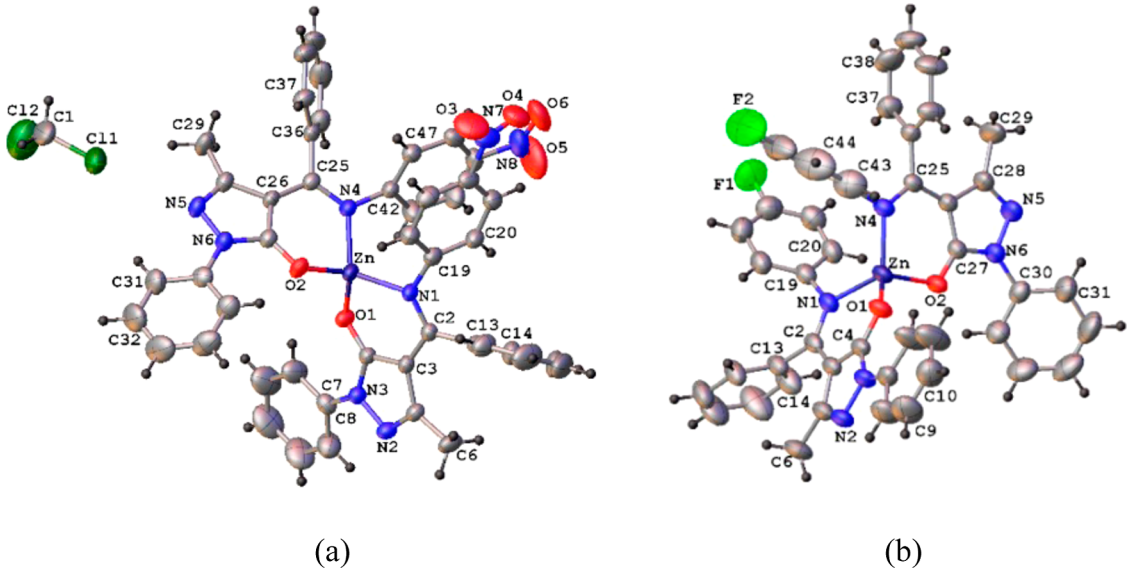

Figure 1. Molecular structure of (a) $[Zn(L^2)_2]\cdot CH_2Cl_2$ (**2**) and (b)) $[Zn(L^4)_2]$ (**4**), with atomic labeling scheme.

Table 1. Selected Bond Distances (Å) and Angles (°) of $[Zn(L^2)_2]CH_2Cl_2$ (2), $[Zn(L^3)_2]$ (3), $[Zn(L^4)_2]$ (4), $[Zn(L^8)_2]$ (8), and $[Zn(L^9)_2]$ (9)

	(2)	(3)	(4)	(8)	(9)
Zn−O(1)	1.929(2)	1.939(2)	1.932(1)	1.948(1)	1.938(2)
Zn−O(2)	1.935(2)	1.949(2)	1.947(1)	1.933(2)	1.941(1)
Zn−N(1)	1.988(2)	2.004(2)	1.997(2)	1.971(2)	2.005(2)
Zn−N(4)	2.007(2)	1.984(2)	1.975(1)	1.998(2)	1.981(2)
O(1)−Zn−O(2)	115.66(9)	115.67(6)	113.99(6)	112.59(6)	113.29(6)
O(1)−Zn−N(1)	97.83(8)	95.62(7)	96.31(6)	98.30(6)	95.81(7)
O(1)−Zn−N(4)	113.78(9)	123.20(7)	120.71(6)	112.47(7)	123.85(7)
O(2)−Zn−N(4)	97.20(8)	97.61(6)	98.28(5)	96.07(7)	97.03(6)
O(2)−Zn−N(1)	117.60(9)	113.22(7)	111.84(6)	123.11(7)	114.14(7)
N(1)−Zn−N(4)	115.94(9)	112.44(7)	116.57(6)	115.08(7)	113.85(7)

These molecules have the potential to adopt four different tautomeric forms (Chart 1), influenced by the electronic characteristics of the R substituents. All proligands exist in the O,NH form, with tautomer A in Chart 1, which was theoretically confirmed (see below). In chloroform, the proton NMR spectra of the compounds exhibit broad signals ranging from 12.86 to 13.24 due to the NH group (see the Supporting Information). This observation aligns with the predominance of the O,NH tautomer A. For the solid state, this configuration has been verified through X-ray structural analysis (discussed below) and IR spectroscopy. In the IR spectra of the proligands, specific bands were recognized, including the asymmetric and symmetric stretching vibrations observed at 1490−1530 and 1325−1331 cm^{-1}, respectively, for the NO_2 group in HL.[2] Additionally, a characteristic stretching mode for the N−N bond, ν(N−N), was identified across all proligands within the frequency range of 1040−1120 cm^{-1}.

The Schiff bases HL^1−HL^9 were deprotonated by potassium hydroxide and then reacted with zinc(II) nitrate hexahydrate in a methanol solution at room temperature. All of the newly synthesized metal complexes demonstrated stability in both air and moisture and exhibited solubility in most organic solvents. They are slightly soluble in alcohols, ethers, and acetonitrile yet insoluble in water. All analytical and spectral data confirmed the formulation of complexes proposed in Scheme 2: they are mononuclear anhydrous $[Zn(HL^n)_2]$ species. Moreover, suitable single crystals for X-ray diffraction analysis have been obtained from slow evaporation of the Zn(II) complexes from methanol solution or a mixture of chloroform and acetonitrile solution. The molecular structures of **2** and **4** are reported in Figure 1.

The IR spectra of the Schiff base ligands and the corresponding complexes provide information about metal−ligand bonding. In the 1500−1650 cm^{-1} range of proligands IR spectra, several medium to strong bands are present due to ν(C═O), ν(C═C), and ν(C═N) modes. In detail, ν(C═O) and ν(C═N) are shifted to lower wavenumbers in the complexes after coordination of the nitrogen and oxygen atoms to zinc. Further evidence of the coordination is given by the appearance of medium to weak low-frequency bands at 520−580 and 430−470 cm^{-1} assigned to ν(Zn−N) and ν(Zn−O), respectively. The thermal behavior of **1**−**9** was analyzed by using thermogravimetric analysis (TGA) under a nitrogen atmosphere at a heating rate of 10 °C per minute (Figure S1). These complexes showed melting points between a temperature range of 150−350 °C. Heating beyond 400 °C resulted in their decomposition, characterized by a series of complex weight losses. The residual mass aligns with the theoretical expectation when considering zinc oxide as the product. In the ^{1}H NMR spectra of complexes **1**−**9** in $CDCl_3$, two sets of signals in ca 10:1 ratio were always observed, the most intense due to the zinc complex and the other corresponding to the

https://doi.org/10.1021/acs.jmedchem.4c01298
J. Med. Chem. 2024, 67, 15676−15690

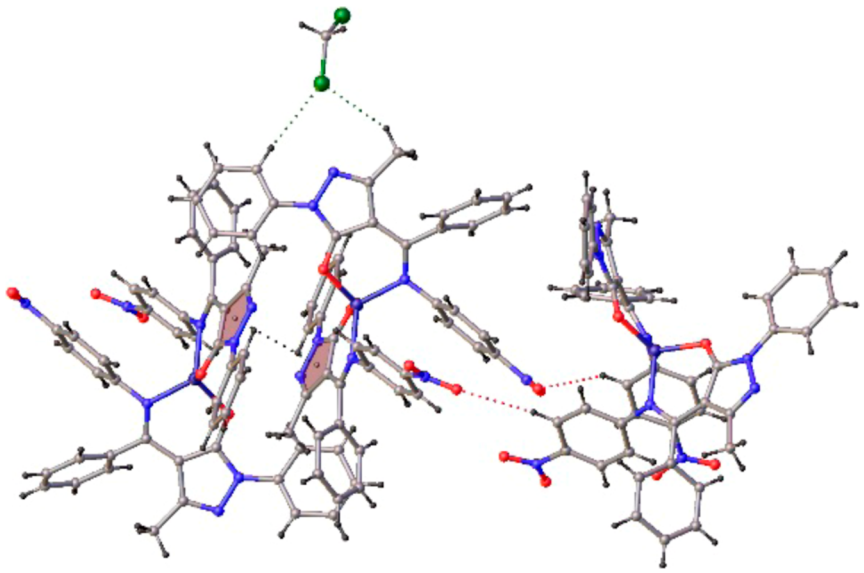

Figure 2. Crystal packing view (approximatively along the *a*-axis) of $[Zn(L^2)_2]\cdot CH_2Cl_2$ (**2**) showing the C−H···Cl, C−H···O, and $\pi-\pi$ intermolecular interactions.

free proligand. This phenomenon has been attributed to the release of the free ligand in chlorinated solution, which has been confirmed by observations of the crystallization mother liquors through powder X-ray diffraction (PXRD) analysis, from UV−vis spectra and from the theoretical studies on the thermodynamic profile of the reaction described below.

Structural Studies. Single crystals of complexes **2**, **3**, **4**, **8**, and **9** suitable for X-ray diffraction structural analysis have been obtained in similar condition, from slow evaporation of a $CH_2Cl_2/CHCl_3$/MeOH solution. Ortep drawing of the molecular structures of **2** and **4**, with atomic labeling scheme is reported in Figure 1 (**3**, **8** and **9** in Figure S2). Relevant bond distances and angles are summarized in Table 1. As shown in Figure 1a, only in the case of complex **2** is one dichloromethane molecule found in the asymmetric unit. In all cases, the Zn(II) ion is tetracoordinated to two chelated deprotonated Schiff base ligands, with distorted tetrahedral geometry (τ4 values in the range of 0.864−0.897).[39]

As observed in related complexes, the Zn−N bond distances (1.971(2)−2.007(2) Å range) are somewhat longer than Zn−O bond distances [1.929(2)−1.949(2) Å range]. All bond lengths and angles are comparable with those already reported for the crystal structure of complex $[Zn(L^6)_2]$ (**6**).[40]

The 3D crystal packing in almost all the Zn(II) derivative molecular structures is characterized by the presence of a weak intermolecular contact of the C−H···N type, involving one of the pyrazole N atoms of the coordinated ligands, able to behave as a hydrogen bond donor. The only exception is found in the case of complex **2**, where the presence of a cocrystallized $CHCl_2$ molecule seems to avoid the proximity of suitable −C−H acceptor groups for at least of the pyrazole N atom (Figure 2). Moreover, the pyrazole ring of the second chelated $[L^2]^-$ ligand establishes $\pi-\pi$ stacking aromatic interactions with the formation of dimeric repeating units.

The $-NO_2$ substituents on the aromatic moiety of the pyrazolone-based Schiff base ligand are found to be involved in weak C−H···O hydrogen bonds. The synthesized microcrystalline powder of both HL^n ligands and $[Zn(L^n)_2]$ complexes has been subjected to routine PXRD analyses, and the powder patterns of complexes **2**, **3**, **4**, **8**, and **9** were compared to the calculated patterns based on single-crystal data (Figure 2).

The comparative analysis confirmed the bulky homogeneity and phase consistency in the case complexes **3**, **4**, **8**, and **9**, while for **2**, slight differences are certainly due to the solvatomorph isolated as single crystals. In the case of all Zn(II) complexes, to prove the eventual dissociation of free ligands from the derived complexes along the crystallization process, though a possible mechanism of hydrolysis, once isolated the single crystals or the crystalline powder, the crystallization solvent was evaporated, yielding a crystalline powder.

The X-ray powder patterns recorded on the so obtained powders in the case of complexes **2** and **4** are reported in Figure 3. As shown in Figure 3a, single crystals of complex **2** are formed along the crystallization process, leaving in the crystallization solution the dissociated ligand in its protonated form and eventually other amorphous species. The same results have been obtained in the case of complexes **3** (Figure S3) and **9** (Figure S4), while for complex **6** (Figure S5), the powder pattern of the product isolated after crystallization is a mixture of HL^6 ligand and the undissociated Zn(II) complex. In the case of complex **4**, the powder isolated from the crystallization solution consists mainly of the intact Zn(II) derivative, and no traces of the dissociated ligand in its protonated form are present (Figure 3b). Similar experiments performed on complexes **1**, **5**, **7**, and **8** have given the same results (Figures S6−S9).

Biological Studies. Then, the cytotoxic activity of the Zn(II) complexes **1**−**9**, as anticancer agents, was investigated in vitro along with mutp53 protein levels, in human cancer cell lines SKB3 and U373 carrying two of the most common mutp53 proteins, R175H and R273H, respectively.[22] mutp53 proteins act as dominant negative on the oncosuppressor function of wild-type p53 and sometimes behave as oncogenes, favoring tumor progression and chemoresistance.[33] p53 is a zinc protein, and previous studies have shown that Zn(II) complexes have been recognized as Zn suppliers in activating wild-type p53 or inhibiting mutp53, reducing tumor growth.[16−25] All Zn complexes showed an IC_{50} value equal

https://doi.org/10.1021/acs.jmedchem.4c01298
J. Med. Chem. 2024, 67, 15676−15690

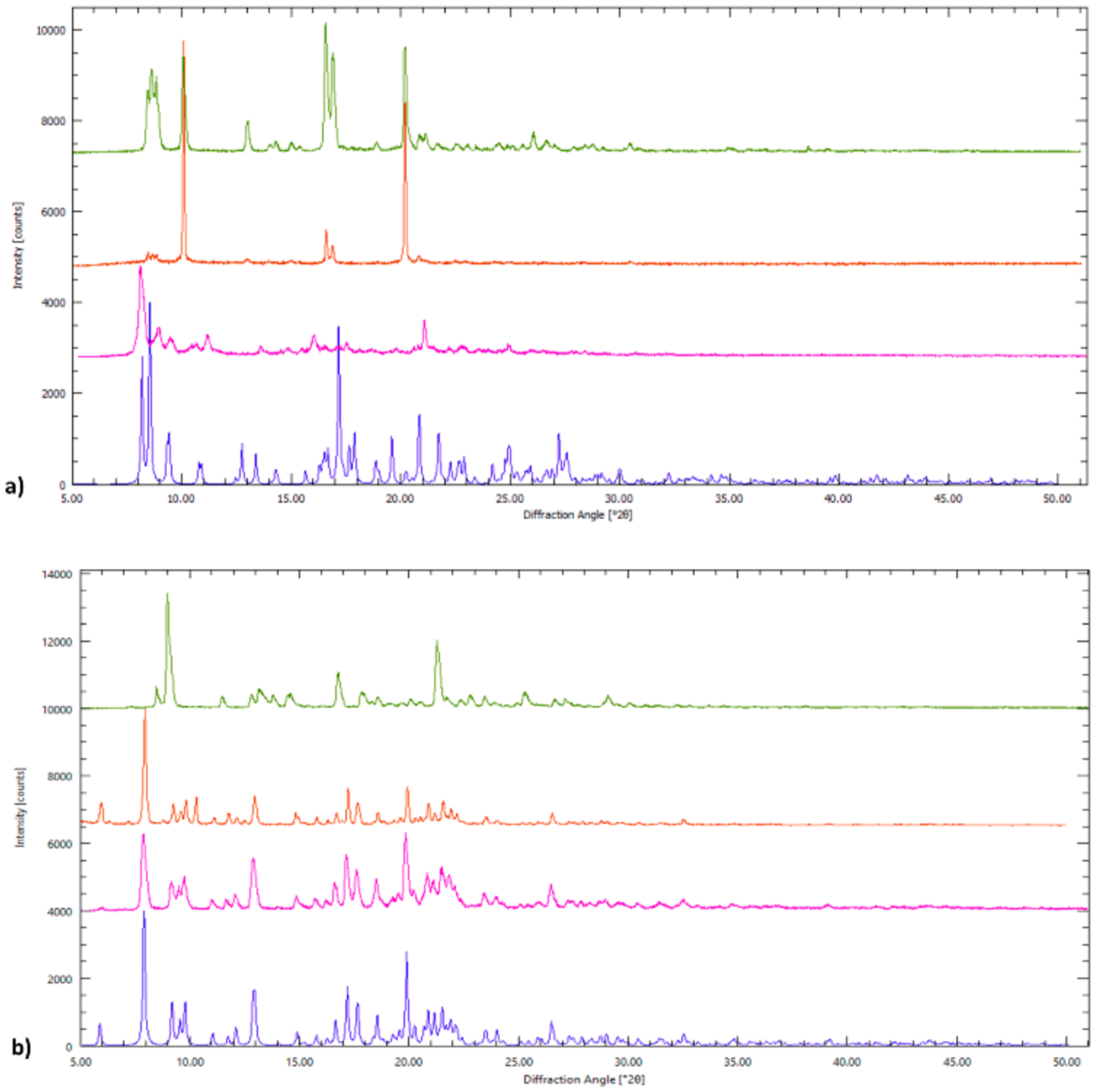

Figure 3. PXRD patterns of (a) $[Zn(L^2)_2]$ (**2**) and (b) $[Zn(L^4)_2]$ (**4**) where the blue line is the simulated pattern from single-crystal data, the pink and the orange lines are the experimental PXRD patterns of the pristine powder samples and the powders isolated from the crystallization solution, and the green line is the PXRD pattern of the respective ligands.

or >200 μM (data not shown), while only the complexes **2**, **3**, **6**, **7**, and **9** showed 20% cell death at 100 μM dose for 48 h, being the effect complex-specific compared to their ligands (data not shown). Therefore, complexes **2**, **3**, **6**, **7**, and **9** were used for further biological assays at the 100 μM dose. The effect of zinc complexes was first evaluated on cancer cell lines by a three-dimensional (3D) culture spheroid proliferation assay.[41,42] 3D tumor spheroids are widely used for assessing drug delivery as they are closer than monolayer cell models to tumor models for clinical treatment and also as they can replicate certain pathological elements of solid tumors such as spatial architecture and hypoxia at the tumor center.[43] Cells cultured in ultralow attachment plates were treated with a 100 μM dose of zinc complexes, and spheroids proliferation was recorded acquiring images after 48 h. Figure 4A shows that complexes **2**, **3**, **6**, **7**, or **9** significantly inhibited spheroids growth of both cell lines, compared to the untreated cells, as evaluated by densitometric analyses (Figure 4B). In addition, the 3D spheroids in the control group appeared denser and with a smooth surface, compared to the zinc-treated spheroids that exhibited important surface breakdown and more detached cells, indicative of a good drug penetration into the spheroid structure.

Then, the effect of zinc complexes on cell migration was investigated by a wound healing assay. The results show that both Mock-treated cell lines rapidly migrated, and the gap significantly narrowed after 36 h, showing a wound healing of about 80 and 75% for, respectively, SKBR3 and U373 cell lines, as evaluated by densitometric analyses (Figure 5A,B). In contrast, fewer cells migrated after the treatment with zinc

https://doi.org/10.1021/acs.jmedchem.4c01298
J. Med. Chem. 2024, 67, 15676−15690

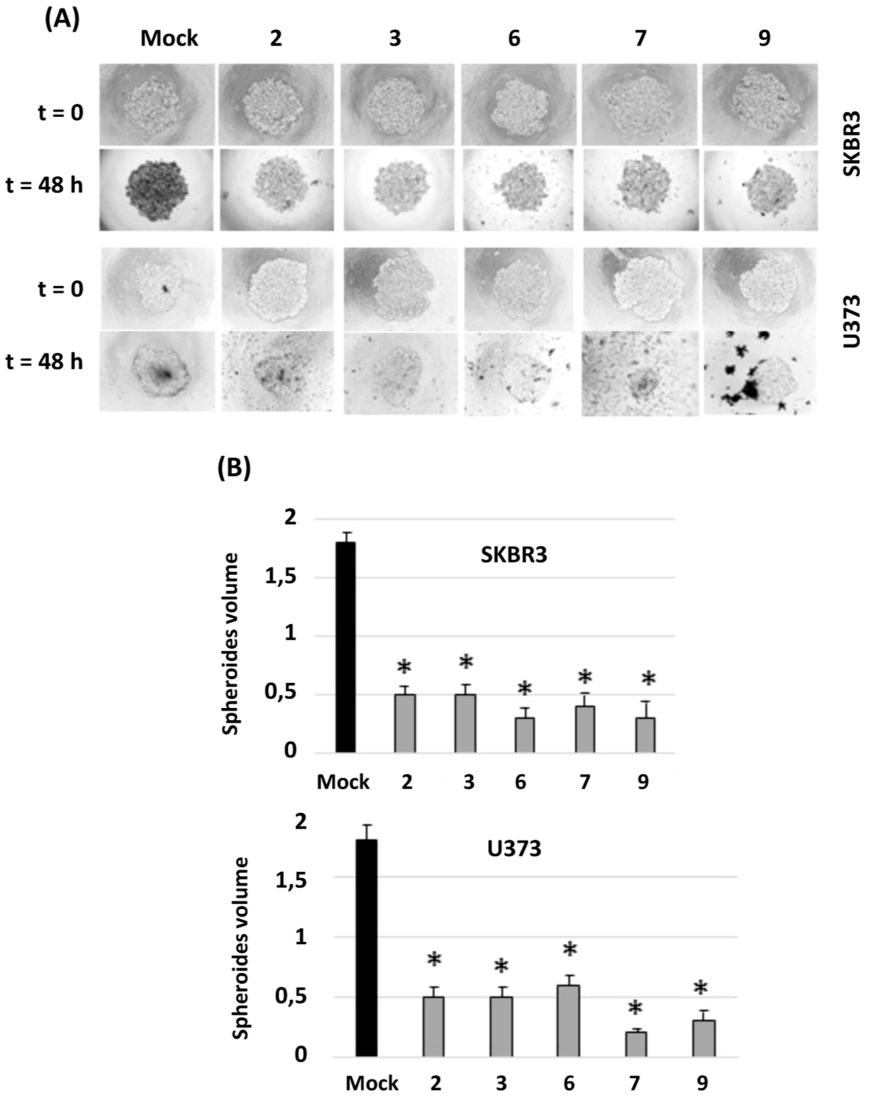

Figure 4. Spheroids growth. (A) Light microscopy images of spheroids of mutp53-carrying U373 and SKBR3 cells, grown on ultralow attachment multiwell plates. Spheroids were Mock-treated or treated with the indicated Zn complexes (100 μM) for 48 h. Tumor spheroid volume was quantified according to the formula: $V = a \times (b2)/2$, where a and b are, respectively, length and width. Representative images of spheroids derived from both cell lines are shown in the upper panels. Spheroid volumes are reported on the bottom panels (B), after densitometric analyses. Histograms represent the fold increase quantified with respect to controls, ±SD * ($p \leq 0.01$), # ($p \leq 0.05$) (single treatments compared to untreated spheroids).

complexes **2**, **3**, **6**, **7**, or **9**, showing larger gaps and reduced ability to heal the wound, indicative of inhibition of the cell migration capacity (Figure 5A,B).

Finally, at the biochemical level, the mutp53 protein expression level was analyzed by Western blot. The results show that while Zn complexes **1**, **4**, **5**, and **8** did not change the mutp53 levels in both cell lines (Figure 6A), complexes **2**, **3**, **6**, **7**, and **9** markedly reduced the mutp53 protein levels, as also evidenced by the densitometric analysis showing the p53/β-actin ratio (Figure 6B). To assess if the reduction of the mutp53 level was at the transcriptional level, mRNA analysis was performed with RT-PCR.

The results show that the p53 mRNA levels were not modified by zinc complexes (data not shown), underlining the hypothesis that the zinc complexes likely affected mutp53 protein stability.

Intriguingly, the reduction of mutp53 levels correlated with the biological effects of reduced cell proliferation, spheroid growth, and migratory capacity induced by treatments with **2**, **3**, **6**, **7**, and **9** as seen above, indicating a likely oncogenic activity for those mutp53 proteins.

These pilot biological results show the promising anticancer activity of zinc complexes **2**, **3**, **6**, **7**, and **9** and the potential effect on reduction of at least two of the most common mutp53 proteins. The molecular mechanisms of mutp53 reduction was not unveiled in this setting; therefore, further studies are necessary to investigate if the mutp53 reduction might depend on autophagy-mediated degradation[44] or by break down of its interplay with chaperones, such as HSP90, that contribute to mutp53 stability[45] or by the interplay with other oncogenic pathways that support mutp53 activity, such as NRF2 or p62.[45−47] Given that mutp53 supports chemoresistance, it is tempting to speculate that complexes **2**, **3**, **6**, **7**, and **9**, by reducing the mutp53 protein levels, might restore chemosensitivity and increase the chemotherapeutic drugs cytotoxicity in combination treatments. Therefore, additional

https://doi.org/10.1021/acs.jmedchem.4c01298
J. Med. Chem. 2024, 67, 15676−15690

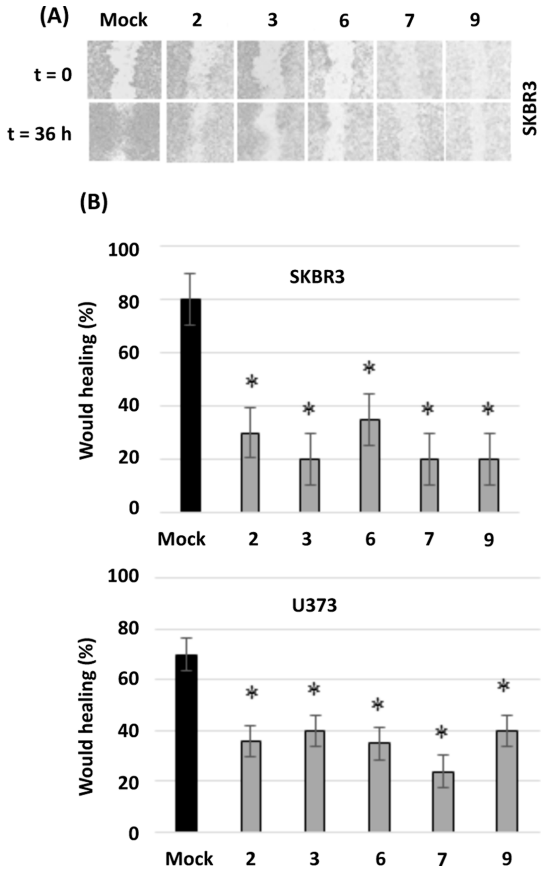

Figure 5. Cell migration following Zn complexes **2**, **3**, **6**, 7, and **9** treatments. (A) Representative images of SKBR3 wound healing after scratch, at time 0 (T0) and after 36 h of the indicated treatments. Untreated cells (Mock) are also shown. (B) Histograms showing the percentage of SKBR3 and U373 cell migration after 36 h without treatment (Mock) or with Zn complexes **2**, **3**, **6**, 7, and **9** treatments, after densitometric analyses. *$p \leq 0.05$ (single treatments compared to Mock).

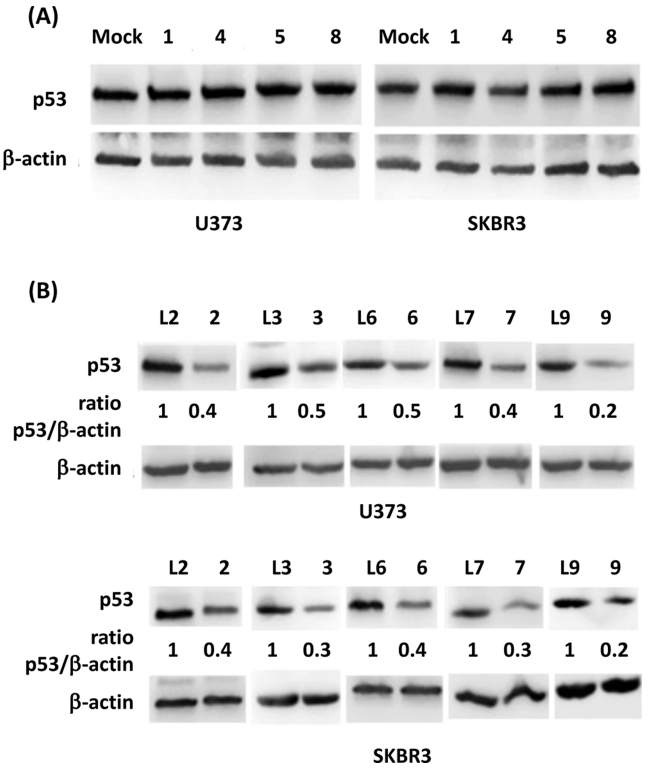

Figure 6. Western blot of SKBR3 and U373 cells following Zn complex treatments. SKBR3 and U373 cells were left untreated or treated with Zn complexes **1**, **4**, **5**, **8** (100 μM for 48 h) (A), or complexes **2**, **3**, **6**, 7, and **9** (B) before assessing p53 levels by Western blot. Anti-β-actin was used as protein loading control. The p53/β-actin ratio, as assessed by densitometric analyses, is indicated below the images.

studies are worth being pursued in combination therapy with classical chemotherapeutic agents. Moreover, these pyrazolone Zn(II) complexes are nontoxic compared to other metals and versatile in terms of ligand exchange reactions,[14] therefore might avoid toxic side effect in the treatment of oncologic patients.

Photophysical Study. All complexes have been characterized in 5% DMSO/PBS buffer to determine their stability under physiological conditions. Before proceeding, however, all ligands and complexes were characterized in dilute dichloromethane solutions, and the results are reported in Table 2.

The ligands exhibit two absorption bands positioned at about 260 and 330 nm (in HL^2 and HL^8, this band appears red-shifted to 372 and 359 nm, respectively) due to $\pi-\pi^*$ transitions localized on the aromatic rings, those without and with the substituent, respectively (Figure S10). The long-wavelength band is particularly asymmetric due to a shoulder in the 370−400 nm range, more pronounced in ligands bearing an electron-donating substituent, and due to an $n-\pi^*$ transition from the nitrogen lone pair toward an aromatic ring. Indeed, while the position of the first band is identical for all of the ligands, the second band (and its shoulder) presents slight differences between the various ligands, being influenced by the presence of the substituent. In ligands with electron-withdrawing groups, the lone pair is less prone to accept the proton of the −OH group and thus remains available for the electronic transition. None of the ligands show emissions. The lack of luminescence is attributed to excited state deactivation via a nonradiative pathway through an intramolecular proton transfer from the OH to the nitrogen lone pair. This proton

Table 2. Absorption Maxima of the Ligands and Complexes in Dichloromethane Solutions

compound	λ_{max}/nm (ε/M^{-1} cm^{-1})
HL^1	330(16120)-285(10500,sh)-259(18070)
HL^2	372(15620)-285(6300,sh)-256(14060)
HL^3	334(26950)-285(13830)-258(26510)
HL^4	323(8230)-285(5600,sh)-259(9470)
HL^5	336(44060)-285(24200,sh)-259(45700)
HL^6	335(8100)-285(6800,sh)-260(10700)
HL^7	333(21550)-285(13300,sh)-259(23880)
HL^8	359(16460)-300(14600,sh)-258(23720)
HL^9	334(21590)-285(11100,sh)-258(21470)
1	330(26150)-286(18000,sh)-259(30290)
2	330(36610)-285(36000,sh)-248(49230)
3	328(28100)-285(22000,sh)-245(35100)
4	333(40100)-285(29500,sh)-245(49250)
5	322(49270)-284(37200,sh)-251(56140)
6	329(28280)-287(19000,sh)-253(31360)
7	329(42190)-278(28200,sh)-246(46330)
8	329(38670)-277(26200,sh)-246(42470)
9	353(22370)-289(22200,sh)-258(33590)

https://doi.org/10.1021/acs.jmedchem.4c01298
J. Med. Chem. 2024, 67, 15676−15690

transfer could be prevented in the solid (due to the crystal packing) and in the complexes (due to coordination with Zn). Therefore, we proceeded with the characterization of the complexes in dichloromethane solution and, subsequently, of the ligands and complexes in solid.

All complexes are stable in dichloromethane solution over 48 h. The absorption spectra of the complexes (Figure S11) are almost superimposable to those of the ligands, with the notable exception of **2** and **8** which appear blue-shifted, and **4** and **9** which are instead red-shifted. In general, coordination with a d^{10} ion leads to a red-shift of the ligand-centered transitions of the complexes with respect to the corresponding ones of the ligands; probably in this case, the coordination leads to an increase in the rigidity of the system, which reduces vibrational losses and could lead to a hypsochromic shift that compensates for the bathochromic effect. All complexes are poorly luminescent, showing a very weak emission band in the range between 535 and 565 nm.[31]

As expected, both ligands and complexes emit in the solid phase (see the emission and excitation spectra of $\mathbf{HL}^1$ and **1** as representative compounds in Figures S12 and S13, which show an emission maximum at 545 and 510 nm, respectively) since the quenching mechanism due to intramolecular proton transfer is blocked in the ligands, while in complexes the rigidity of the solid increases the efficiency of the radiative de-excitation pathways. A shoulder is evident in the excitation spectrum of HL,[1] which disappears when the ligand coordinates with Zn^{2+}. As previously stated, characterization under physiological conditions in PBS buffer requires that the compounds be dissolved in a 5% mixture in DMSO since they are poorly soluble in water. For this reason, absorption spectra of anhydrous DMSO solutions of the compounds were collected (Figure S14). The spectra of the ligands are superimposable to those collected in dichloromethane, with the exception of HL^8 which appears red-shifted. Instead, the spectra of the complexes in DMSO are blue-shifted compared to those recorded in dichloromethane, with the exception of **9** which is red-shifted. As expected, the ligands do not emit in DMSO, while a weak emission is detected from the complex solutions, with a maximum ranging from 522 (complex **1**) to 591 nm (complex **9**).

The stability of the compounds was monitored by collecting absorption spectra at $t = 0$ and $t = 24$ h. The anhydrous DMSO solutions are stable for 24 h; in the case of DMSO/buffer solutions, while the ligands are stable, the absorption spectra of all the complexes show a dramatic variation over the considered time span (Figure S15). Indeed, although DMSO/buffer solutions show a clouding that makes the identification of the absorption bands quite difficult, the shape of the spectra at $t = 24$ h indicates the breakdown of the complex. Only in the spectra of some complexes (**4**, **6**, **8**, and **9**), it was possible to identify absorption maxima, which appear invariably red-shifted with respect to the absorption bands observed at $t = 0$, and similar to the absorption spectra of the protonated ligands. In the case of complex **8**, however, it was possible to collect the precipitate after 24 h, dry it, and redisperse it in DMSO. The absorption spectrum of the precipitate was compared both with that of the starting complex and that of its ligand, i.e., **8** and HL^8, respectively, all dissolved in DMSO. This comparison is shown in Figure 7, from which it can be noted that the precipitate coming from the DMSO/buffer solution corresponds to the protonated ligand, formed following the hydrolysis of the complex, and which, being poorly soluble in the aqueous medium, precipitates.

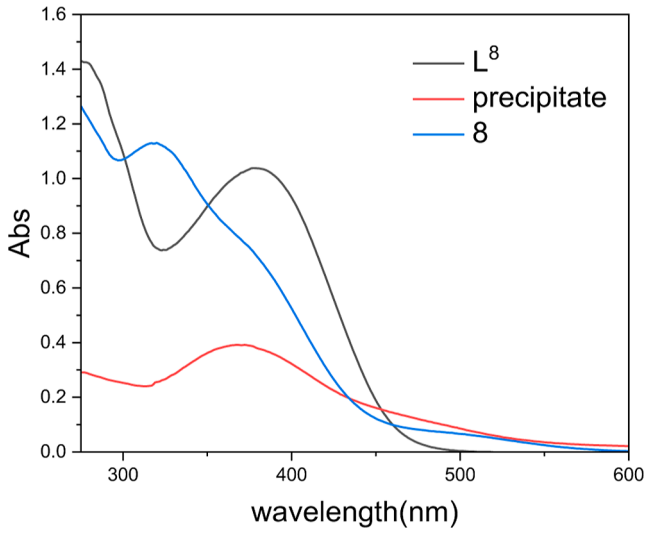

Figure 7. Absorption spectra in DMSO solution of HL^8, **8**, and of the precipitate collected after 24 h from the DMSO/buffer solution of **8** (see the text).

Theoretical Studies. The proligands HL^n ($n = 1-9$) and their possible tautomers were investigated using density functional theory (DFT) at the B3LYP/6-311G* theoretical level. Initially, we selected as a model the compound HL^1 and their possible tautomers **A**–**D** (Chart 2) to be optimized (Table S1).

From an energetic point of view, tautomers **C** and **D** are clearly destabilized by 21.1 and 14.8 kcal/mol (relative $\Delta G_{\text{gas-phase}}$) with respect to the most stable form **A**, while the $\Delta G_{\text{gas-phase}}$ destabilization of **B** is lower (8.4 kcal/mol). After this result, only the most stable tautomers **A** (form O,NH) and **B** (form OH,N) were optimized for all proligands HL^n ($n = 1-9$). The resulting structures for both forms and their relative energies are collected in Table S2. For all proligands, tautomer **A** was the most stable in the gas phase with energy differences with respect to **B** in the range of 7.3–9.8 kcal/mol (see Table S2 for additional details). Selected bond distances of tautomer **A** for all proligands HL^n ($n = 1-9$) are collected in Table S3. The electronic nature of the R substituent in the para position influences this energy difference between tautomers **A** and **B**. In fact, the graphical representation of the σ Hammett parameter versus the relative electronic energy difference ΔE is linear (Figure 8, R^2 correlation coefficient of 0.936). Electron donor substituents increase this energy difference ΔE, producing a major stabilization of the O,NH tautomer (**A**), while electron-withdrawing substituents decrease the ΔE value. The calculated ^{1}H NMR chemical shifts for the NH (tautomer **A**) or OH (tautomer **B**) signals of each tautomer of the HL^n proligands in a $CHCl_3$ solution gave mean values of 12.90 and 14.24 ppm, respectively. The former fits quite well with the experimental mean value of 12.89 ppm, corroborating the existence in a solution of tautomer **A** in these compounds.

The ligands $[L^n]^-$ ($n = 1-9$) were also optimized, and the resulting structures are shown in Figure S16. Selected bond distances within the atoms involved in the metallacycle moiety when bonded to the zinc center are listed in Table S4.

https://doi.org/10.1021/acs.jmedchem.4c01298
J. Med. Chem. 2024, 67, 15676−15690

Chart 2. Possible tautomers A–D of ligand HL[1].

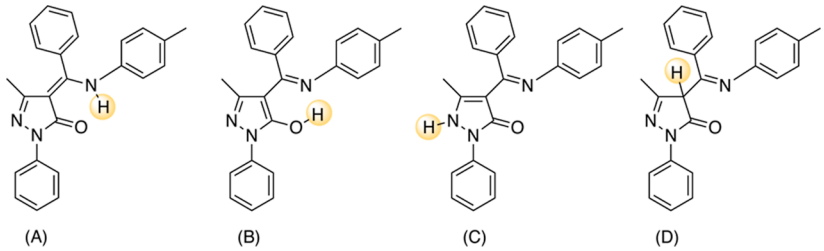

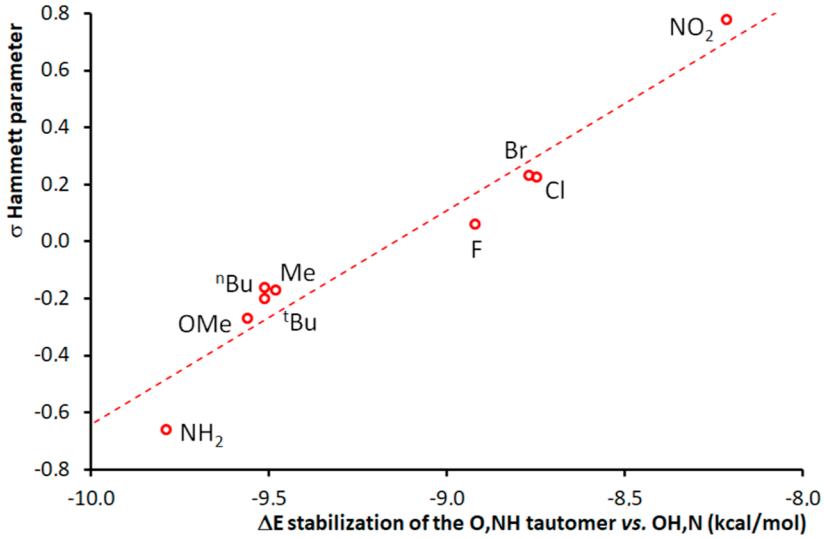

Figure 8. Correlation between the relative difference in electronic energy for the stabilization of the O,NH tautomer with respect to the OH,N form of the proligands HL^n and the σ Hammett parameter for the p-substituent R.

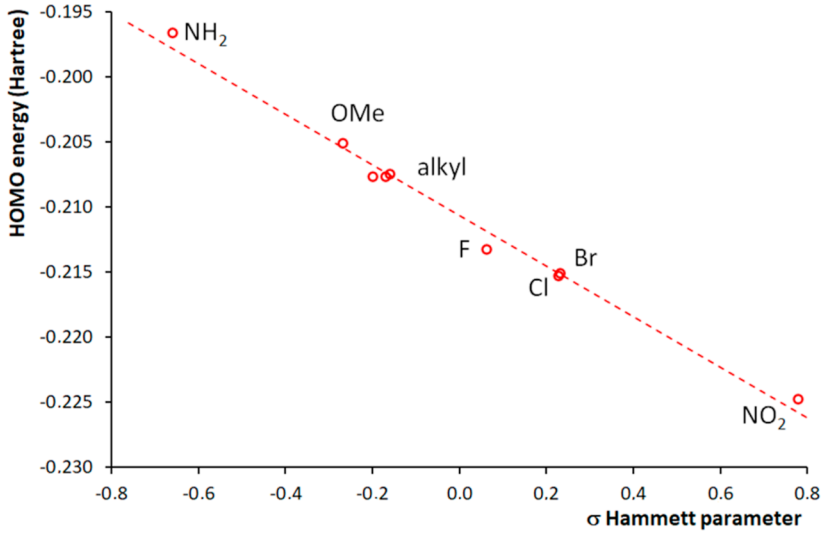

Figure 9. Relationship between the HOMO energy of complexes **1**–**9** and the σ Hammett parameter for the p-substituent R.

The C═O bond distances of the anions (mean value 1.228 Å) remain essentially unchanged with respect to those of the parent proligands (mean value 1.241 Å).

By contrast, the C⋯N lengths (mean value 1.306 Å) are shorter than those of the parent HL^n (mean value 1.352 Å). The delocalization is also observed in the CC distances, where the alternance C═C and C–C observed in compounds HL^n (Table S3, mean values of 1.390 and 1.465 Å, respectively) disappears in the anions [L^n]$^-$ (Table S4, mean values of 1.430 and 1.455 Å, respectively). A careful analysis of these bond distances (Table S4) shows smooth relationships with the σ Hammett parameter of the *p*-substituent R. In fact, when the electron donor capacity of R increases, the C═O distances gradually become longer and the C⋯N shorter (Figure S17a,b). Similar correlations are found for the CC bond distances (Figure S17c,d). To gain information about the coordination capabilities of these ligands in zinc complexes **1**–**9**, their MOs were obtained from the single-point calculation

https://doi.org/10.1021/acs.jmedchem.4c01298
J. Med. Chem. 2024, 67, 15676–15690

Scheme 3. Proposed Mechanism for the Aquation of 1−9

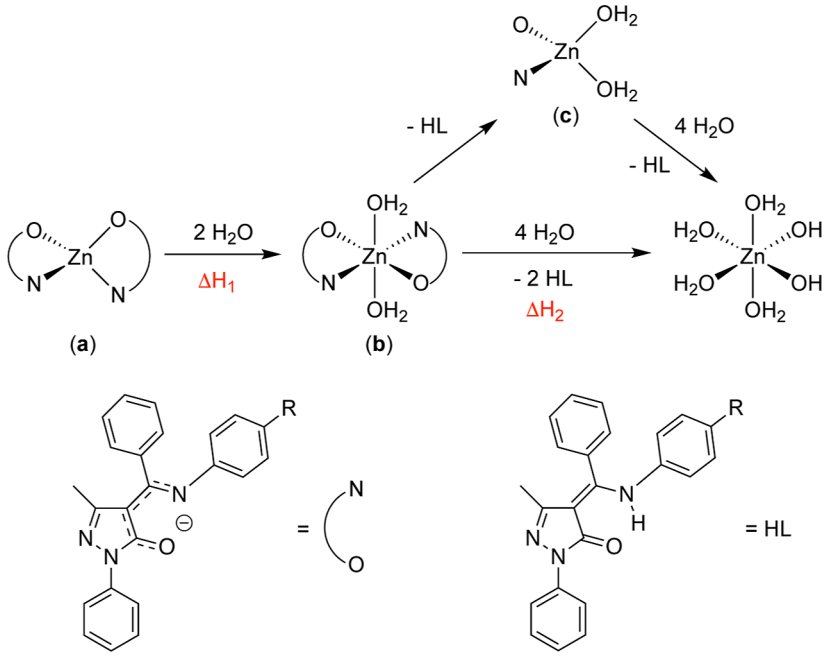

of the HL^n ligand with the geometry found in the optimization of their respective complexes (see below). The ligands are characterized by a HOMO constituted for the π part of the pyrazolone ring plus the contributions of perpendicular p orbitals of the O and N atoms (see Figure S18). The out-of-phase and in-phase combinations are clearly detected in HOMO − 1 and HOMO − 3, respectively, which are the MOs involved in σ-coordination to the metal center (Figure S18).

The optimized structures of zinc complexes **1−9** are shown in Figure S19, while selected structural parameters are collected in Table S5. The selected combination of method and basis sets provides a satisfactory structural description of these complexes, as it is deduced from the comparison of the structural parameters of **2**, **4** and **6** with those determined by X-ray diffraction (see Table S6). The calculated Zn−O and Zn−N bond lengths fall in the ranges of 1.961−1.970 and 1.989−1.999 Å, respectively. The C⩵N (mean value of 1.325 Å) and C⩵O (mean value of 1.276 Å) distances agree with delocalization within the metallacycle and are slightly longer than those calculated for their corresponding anions $[L^n]^-$. The HOMOs of complexes **1−9**, as shown in Figure S20, are characterized by the contributions of the HOMOs of the two ligands $[L^n]^-$. The exceptions are the HOMOs of complexes **6** and **8**, which contain R electron-donating groups (OMe and NH_2, respectively), in which additional participation of the phenyl ring with the para R substituent appears (Figure S20). Interestingly, the energy of the HOMO is controlled by the electronic properties of the R group. Figure 9 shows the correlation between the σ Hammett parameter for p-substituent R and the HOMO energy of the zinc complexes.

The presence of an electron donor group (such as NH_2 in **8**) destabilizes the HOMO, and the opposite situation occurs with electron-withdrawing groups (such as NO_2 in **2**), which makes the HOMO more stable.

To gain information about the aquation of complexes **1−9** with the aim of explaining their biological activity, the thermodynamic profile of this reaction was theoretically analyzed. The proposed mechanism is schematically depicted in Scheme 3, while the optimized structures of the intermediates are shown in Figure S20.

The first step is the coordination of water as two additional ligands to give complexes $[Zn(L^n)_2(H_2O)_2]$ (n = **1a−9a**). These intermediates display slightly distorted octahedral structures, with the water ligands occupying *trans* positions. A similar structural configuration was encountered in related zinc complexes reported by us.[48] The second step is the hydrolysis of one of the coordinated $(L^n)^-$ ligands with its elimination as a neutral HL^n species and formation of a hydroxide ligand. These HL^n precursors were identified by PXRD in the mother liquors of crystallization (see above). The resulting intermediates $[Zn(L^n)(OH)(H_2O)]$ (n = **1b−9b**) show a distorted tetrahedral structure (Figure S21). Subsequent hydrolysis of the second $(L^n)^-$ ligand and additional coordination of water produce complete aquation and the formation of the complex $[Zn(OH)_2(H_2O)_4]$.

The gradual release of Zn(II) ions from complexes **1−9** could be considered to be a crucial step in the observed biological activity of these complexes. However, the observed activity cannot be related to the electronic or steric properties of the R substituent of the $(L^n)^-$ ligands (Scheme 1). The ease with which the zinc ion is released from the complex is related to the ΔH energy values of the hydrolysis reactions of the ligands, and for this reason, the ΔH_1 and ΔH_2 values of aquation were calculated (Scheme 3). Interestingly, the ΔH_2 parameter provides a boundary that discriminates biologically active complexes from those that do not exhibit activity (see Table S7). Furthermore, the graphical representation of ΔH_1 versus ΔH_2 allows us to generate areas of activity and no activity that fits reasonably well with the observed biological behavior (Figure S22).

CONCLUSIONS

Herein, we have presented the coordination chemistry of a series of 4-aminoalkylidene-5-pyrazolone molecules, their derived homoleptic Zn(II) complexes, and correlation studies on their structural, photophysical, and bioactivity properties

https://doi.org/10.1021/acs.jmedchem.4c01298
J. Med. Chem. 2024, 67, 15676−15690

with the different substituents on the aromatic moiety of the pyrazolone-based Schiff base ligands coordinated to the Zn(II) ion. The efficacy of the Zn(II) complexes **1**−**9** as anticancer agents and their cytotoxicity toward human cancer cell lines carrying mutp53 was also investigated. p53 protein has been shown to be Zn-dependent, which might be its unique vulnerability, and its mutations, which are mostly zinc-deficient, are associated with tumor progression and chemo-resistance.[22,24,25] The results presented in this study show that while Zn complexes **1**, **4**, **5**, or **8** did not change the mutp53 levels in both cell lines, complexes **2**, **3**, **6**, **7**, or **9**, markedly reduced the mutp53 protein levels. In agreement, the reduction of mutp53 levels correlated with the biological effects of tumor cell growth reduction and wound healing inhibition. Previous studies have exploited zinc supplementation as a therapeutic strategy to restore wild-type p53 function or degrade mutp53 protein.[49] Therefore, the development of novel anticancer Zn complexes might be valuable for p53 targeting. In this regard, as the pyrazolone Zn(II) complexes presented in this study are nontoxic compared to other metals and versatile in terms of ligand exchange reactions,[14] they are good candidates in combination therapy to avoid toxic side effect in the treatment of oncologic patients. Absorption spectroscopy shows that the complexes are stable in anhydrous solvents, but in the presence of water, they all dissociate, releasing the ligand. X-ray powder patterns obtained by evaporating the crystallization solvent from the solution prepared by dissolving isolated single crystals or crystalline powder of the various complexes have shown that they follow different hydrolysis kinetics. To gain information about the aquation of complexes and with the aim of explaining their biological activity, the thermodynamic profile of this reaction was theoretically analyzed; this reaction consists of two steps: the first is the attachment of two water molecules to the zinc atom, and the second is the release of the ligands. The gradual release of Zn(II) ions from complexes **1**−**9** could be considered a crucial step in the observed biological activity of these complexes. The ease with which the zinc ion is released from the complex is related to the ΔH energy values of the hydrolysis reactions of the ligands, and for this reason, the ΔH_1 and ΔH_2 values of aquation were calculated. Interestingly, the ΔH_2 parameter provides a boundary that discriminates between biologically active complexes and those that do not exhibit activity. In summary, these Zn(II) homoleptic derivatives can be considered promising zinc chaperones in clearing mutp53 and likely restoring chemo-sensitivity although additional studies are necessary to strengthen this issue as well as to evaluate the potential effect also in activating wild-type p53 and spare normal cells.

EXPERIMENTAL SECTION

Materials and Methods. All reagents were purchased from Aldrich and used without further purification. All solvents were purified by conventional methods and stored under nitrogen. All reactions and manipulations for the syntheses of proligands HL^n and their interactions with zinc acetate dihydrate were carried out in the air. The samples for microanalyses were dried in vacuo to constant weight (20 °C, ca. 0.1 Torr). Elemental analyses (C, H, and N) were performed in-house with a Fisons Instruments 1108 CHNS−O Elemental Analyzer. Melting points are uncorrected and were recorded on a STMP3 Stuart scientific instrument and on a capillary apparatus. IR spectra were recorded from 4000 to 200 cm^{-1} with a PerkinElmer Spectrum 100 FT-IR instrument. ^1H, ^{19}F, and ^{13}C NMR spectra were recorded with a 500 Bruker AscendTM (500 MHz for ^1H, 470.6 for ^{19}F, and 125 MHz for ^{13}C) instrument operating at room temperature relative to TMS. X-ray diffraction patterns of the powder samples were acquired on a Bruker D2-Phaser equipped with Cu K_α radiation (λ = 1.5418 Å) and a Lynxeye detector, at 30 kV and 10 mA, with a step size of 0.01° (2θ). The obtained diffractograms were analyzed with PROFEX 5.3.0 diffraction free software.[50]

Synthesis of Proligands HL^n. *HL^1*. The proligand HL^1 was synthesized by mixing (5-hydroxy-3-methyl-1-phenyl-1*H*-pyrazol-4yl)(phenyl)methanone (m.w. 278.3, 278 mg, 1 mmol) and 4-methylaniline (m.w. 107.1, 107 mg, 1 mmol) in ethanol at reflux and stirring the reaction mixture for 4 h. The product precipitated from the hot solution as the reaction proceeded. After it was cooled, the product was filtered off and recrystallized from ethanol to give a yellow solid (323 mg, 88%). HL^1 is soluble in DMSO, DMF, acetone, chlorinated solvents, and slightly soluble in acetonitrile, methanol, ethanol, diethyl ether, and petroleum ether. mp: 202−204 °C. Anal. Calcd for $C_{24}H_{21}N_3O$ (m.w. 367.4): C, 78.45; H, 5.76; N, 11.44%. Found: C, 78.28; H, 5.56; N, 11.25%. IR (cm^{-1}): 3077w ν(C−H aromatics), 1614s ν(C═O), 1585s, 1569s ν(C═C), 1533 ν(C═N). ^1H NMR ($CDCl_3$ with 0.05% v/v TMS, 500 MHz, 298 K): δ_H 1.57 (s, 3H, H15), 2.23 (s, 3H, H20), 6.70 (d, 2H, H18,18′), 6.93 (d, 2H, H17,17′), 7.17 (t, 1H, H9), 7.35 (t, 2H, H8), 7.42 (d, 2H, H13,13′), 7.49 (m, 3H, H14,14′, H15), 8.03 (d, 2H, H7,7′), 12.94 (sbr, 1H, N3−H). ^{13}C NMR ($CDCl_3$, 125 MHz, 298 K): δ_C 16.2 (C15), 21.0 (C20), 101.3 (C4), 119.5 (C7), 123.9 (C18,18′), 124.7 (C8,8′), 128.7 (C9), 129.0 (C12,12′), 129.1 (C13,13′,14), 129.8 (C17,17′), 130.6 (C17), 131.8 (C19), 135.0 (C11), 136.2 (C6), 139.1 (C16), 148.3 (C3), 162.5 (C10), 165.9 (C5). {^1H,^{15}N}gs-HSQC NMR ($CDCl_3$, 51 MHz, ^3J(N−H) = 3 Hz, 298 K): δN 133.4 (*N*3). {^1H,^{15}N} gs-HMBC NMR ($CDCl_3$, 51 MHz, ^3J(N−H) = 3 Hz, 298 K): δN 191.0 (*N*1), 284.2 (*N*2), 133.4 (*N*3).

The other proligands HL^n (n = 2−9) were prepared similar to HL.[1] Purity of all proligands is >95%, as confirmed by elemental analyses. Their analytical and spectral data are reported in the Supporting Information. The NMR spectra of all ligands are reported in Supporting Information (Figures S23−S59).

Synthesis of Zn(II) Complexes 1−9. *$[Zn(L^1)_2]$ (1)*. Complex **1** was synthesized by mixing $Zn(NO_3)_2{\cdot}6H_2O$ (0.029 g, 0.1 mmol) and the deprotonated proligand HL^1 (0.073 g, 0.2 mmol) in 20 mL of methanol. A slightly yellow solid slowly precipitated from the solution. After 2 h stirring at room temperature, the suspension was filtered off, and the precipitate was washed with cold MeOH and dried to constant weight under reduced pressure. It was recrystallized from chloroform/acetonitrile. Yield 654 mg, 82%. It is soluble in chlorinated solvents and slightly soluble in DMSO, DMF, acetone, acetonitrile, ethanol, methanol, diethyl ether, and petroleum ether. mp: 338−340 °C. Elemental Analyses Calcd. for $C_{48}H_{40}N_6O_2Zn$ (m.w. 798.3): C, 72.22; H, 5.05; N, 10.53%. Found: C, 73.02; H, 4.88; N, 10.16%. IR (cm^{-1}): 3065w ν(C−H aromatics), 1601s, 1590m, 1572m ν(C═C), 1554s ν(C═C), 1527m ν(C═N), 1469s, 1435s, 1056m ν(N−N). ^1H NMR ($CDCl_3$ with 0.05% v/v TMS, 500 MHz, 298 K): δ_H 1.59 (s, 6H, H15), 2.26 (s, 6H, H20), 6.68 (d, 4H, H18), 6.96 (d, 4H, H17), 7.20 (t, 2H, H9), 7.36 (t, 4H, H8), 7.37 (d, 4H, H13), 7.47 (m, 6H, H14, H15), 8.04 (d, 4H, H7). ^{13}C NMR ($CDCl_3$, 125 MHz, 298 K): δ_C 15.9 (C15), 20.8 (C20), 101.1 (C4), 119.3 (C7), 121.7 (C8), 124.5 (C18), 127.7 (C9), 128.2 (C12), 128.8 (C13,14), 129.5 (C17), 130.3 (C19), 135.8 (C11), 138.8 (C6), 143.9 (C16), 149.5 (C3), 163.1 (C10), 172.8 (C5). {^1H,^{15}N}gs-HSQC NMR ($CDCl_3$, 51 MHz, ^3J(N−H) = 3 Hz, 298 K): δN 135.6 (*N*3). {^1H,^{15}N} gs-HMBC NMR ($CDCl_3$, 51 MHz, ^3J(N−H) = 3 Hz, 298 K): δN 274.6 (*N*2), 285.8.2 (*N*2).

The other Zn(II) complexes **2**−**9** were prepared similar to those of **1**. Purity of all zinc complexes is >95%, as confirmed by elemental analyses. Their analytical and spectral data are reported in the Supporting Information. The NMR spectra of all complexes are reported in Supporting Information (Figures S60−S96).

X-ray Crystallographic Analysis. Single-crystal X-ray diffraction data of complexes **2** and **4** were collected at room temperature with a Bruker-Nonius X8APEXII CCD area detector system equipped with a graphite monochromator with radiation of Mo Kα (λ = 0.71073 Å). For complexes **3**, **8**, and **9**, data were collected at 100(2) K with

https://doi.org/10.1021/acs.jmedchem.4c01298
J. Med. Chem. 2024, 67, 15676−15690

radiation Mo Kα (λ = 0.71073 Å) on a Bruker D8 VENTURE diffractometer. In all cases, data were integrated, corrected from absorption effects, and scaled with SAINT and SADABS programs.[51−53] Structures were solved by direct methods and refined by full-matrix least-squares based on F^2 through the SHELX and SHELXTL software package.[54,55] The CH_2Cl_2 cocrystallized molecule in complex **2** is found disordered in two position. The relative occupancies of the two disorder components were refined fixed, constraining their sum to unity,[56] at values of 0.7 and 0.3, respectively. All non-hydrogen atoms were refined anisotropically, hydrogen atoms were included at geometrically calculated positions, and refined details of data collection and structure refinements are reported in Table S8.

Biological Studies. *Cell Culture.* Human breast cancer SKBR3 (carrying p53R175H mutation) and glioblastoma U373MG (carrying p53R273 mutation) cell lines were grown, respectively, in Dulbecco's modified Eagle's medium and RPMI-1640 medium (Life Technologies-Invitrogen, Eggenstein, Germany), supplemented with 10% heat-inactivated fetal bovine serum (Corning, NY, USA) plus L-glutamine/streptomycin (100 μg/mL) (Corning, NY, USA), in a humidified atmosphere with 5% CO_2 at 37 °C. The cells underwent routine testing to ensure that they were mycoplasm negative. Cells were treated with the zinc-complexes or were Mock-treated as control.

3D Spheroids Proliferation Assay. The 3D spheroids were obtained into ultralow attachment cell culture multiwell plates (96 well, Corning), as previously reported.[41,57] When spheroids reached approximate size of 300−500 μm (about 4 days after plating), they were treated with the zinc complexes (10, 50, and 100 μM) or Mock-treated. Spheroids images were acquired with a Nikon Eclipse TS100 microscope equipped with a Nikon ELWD camera (Nikon Instrument Europe BV, Amsterdam, The Netherlands) every 24 h. The formula to evaluate the spheroid volume was: $V = a \times (b2)/2$, where a and b are, respectively, length and width.

Wound Healing Assay. Cells were plated in triplicates in 24-well plates at a density of 180,000 cells per well, forming a single cell layer the day after. At 24 h after plating, cells were scratched through the monolayer using a 1000 μL pipet tip. Cells were rinsed to remove cellular debris, and serum-free medium was added before placing plates in an IncuCyte Live Analysis Incubator (Essen BioScience, Ann Arbor, MI, USA) at 37 °C. The IncuCyte live-cell imaging enables noninvasive, full kinetic measurements of cell growth based on area (confluence) metrics. Images of the wells were taken every 6 h, and migration assays were analyzed until 66 years later. For drug treatment, media containing the specific concentration of the Zn complexes were added at the time of the scratch. Data were analyzed by using the IncuCyte software v2022A package (Essen BioScience, Ann Arbor, MI, USA). The percentage (%) of migration was calculated using the following formula: 100 − (final area/initial area × 100%).

Western Blot Analysis. Cell pellets were lysed in lysis buffer (50 mM Tris−HCl, pH7.5, 150 mM NaCl, 5 mM EDTA, 150 mM KCl, 1 mM dithiothreitol, 1% Nonidet P-40) (all from Sigma-Aldrich) and a mix of protease inhibitors (CompleteTM, Mini Protease Inhibitor Cocktail, Merk, Life Science S.r.l., Milan, Italy). The protein concentration was determined with the BCA Protein Assay (BioRad, Hercules, CA, USA) to load equal amounts of total cell extracts on 9−18% SDS−polyacrylamide gel (PAGE) (Bio-Rad) electrotrophoreses. After blotting to polyvinylidene difluoride membranes (Millipore Corporation, Billerica, MA, USA), unspecific sites were blocked with 5% nonfat powdered milk (Sigma-Aldrich) in 0.05% Tween-20 (v/v in TBS). Membranes were then incubated with mouse monoclonal anti-p53 (DO-1) (1:1000) (sc-126) and mouse monoclonal antiactin antibody (Ab-1) (JLA20) (1:10.000) (Calbiochem, #CP01) primary antibodies. Antimouse immunoglobulin-G-horseradish peroxidase (IgG-HRP) secondary antibody (BioRad, #172-1011) was used. Enzymatic signals were visualized by chemiluminescence (ECL Detection system, Amersham GE Healthcare, Milan, Italy, #RPN2106), according to the manufacturer's protocol. Quantification of the protein bands was assessed by densitometric analysis using ImageJ software (http://imagej.nih.gov) and relative band intensity normalized to β-actin signals.

Spectroscopic Studies. Spectrofluorimetric grade solvents (Merck KGaA, Darmstadt, Germany) were used for the photophysical investigations in solution at room temperature. A PerkinElmer Lambda 900 spectrophotometer was employed to obtain the absorption spectra. Steady-state emission spectra were recorded on a HORIBA Jobin-Yvon Fluorolog-3 FL3−211 spectrometer equipped with a 450 W xenon arc lamp, double-grating excitation and single-grating emission monochromators (2.1 nm/mm dispersion; 1200 grooves/mm), and a Hamamatsu R928 photomultiplier tube. Emission and excitation spectra were corrected for the source intensity (lamp and grating) and emission spectral response (detector and grating) by standard correction curves. Solid samples are prepared by placing microcrystalline powder between two quartz windows, and spectra were recorded in an instrumental front-face geometry.

Computational Details. The electronic structure and geometries of the proligands HL″, their tautomers, their corresponding anions $[L'']^-$ and the Zn complexes **1**−**9** were calculated using DFT at the B3LYP level with the 6-311G* basis set.[58,59] Geometry optimizations were performed with the actual compounds without symmetry restrictions. Frequency calculations were performed at the same level of theory to identify all of the stationary points as minima (zero imaginary frequencies). The GIAO method was used for the NMR calculations, which were carried out at the 6-311++G** level of theory. The computed IR spectra were scaled by a factor of 0.96.[60,61] The DFT calculations were performed using the Gaussian 09 suite of programs.[62] The coordinates of all optimized compounds are reported in Table S9.

■ ASSOCIATED CONTENT

Supporting Information

The Supporting Information is available free of charge at https://pubs.acs.org/doi/10.1021/acs.jmedchem.4c01298.

CCDC deposition number 2359977−2359981 for X-ray crystal structures of complexes $[Zn(L^2)_2]$ (**2**), $[Zn(L^3)_2]$ (**3**), $[Zn(L^4)_2]$ (**4**), $[Zn(L^8)_2]$ (**8**), and $[Zn(L^9)_2]$ (**9**); TGA curves; NMR spectra; PXRD patterns; absorption and emission spectra; and data from DFT studies (PDF)

Molecular formula strings (CSV)

■ AUTHOR INFORMATION

Corresponding Author

Fabio Marchetti − *ChIP Research Center, School of Science and Technology, University of Camerino, 62032 Macerata, Italy;* orcid.org/0000-0001-5981-930X; Email: fabio.marchetti@unicam.it

Authors

Sonila Xhafa − *ChIP Research Center, School of Science and Technology, University of Camerino, 62032 Macerata, Italy*

Corrado Di Nicola − *ChIP Research Center, School of Science and Technology, University of Camerino, 62032 Macerata, Italy;* orcid.org/0000-0002-0958-6103

Alessia Tombesi − *ChIP Research Center, School of Pharmacy, University of Camerino, 62032 Macerata, Italy;* orcid.org/0000-0002-2765-4587

Riccardo Pettinari − *ChIP Research Center, School of Pharmacy, University of Camerino, 62032 Macerata, Italy;* orcid.org/0000-0002-6313-4431

Claudio Pettinari − *ChIP Research Center, School of Pharmacy, University of Camerino, 62032 Macerata, Italy;* orcid.org/0000-0002-2547-7206

Francesca Scarpelli − *MAT-InLAB, Dipartimento di Chimica e Tecnologie Chimiche, Università della Calabria, 87036 Cosenza, Italy;* orcid.org/0000-0002-3461-0478

Alessandra Crispini − *MAT-InLAB, Dipartimento di Chimica e Tecnologie Chimiche, Università della Calabria, 87036 Cosenza, Italy*
Massimo La Deda − *MAT-InLAB, Dipartimento di Chimica e Tecnologie Chimiche, Università della Calabria, 87036 Cosenza, Italy;* orcid.org/0000-0002-8611-5575
Angela Candreva − *MAT-InLAB, Dipartimento di Chimica e Tecnologie Chimiche, Università della Calabria, 87036 Cosenza, Italy*
Alessia Garufi − *Department of Research and Advanced Technologies, IRCCS Regina Elena, National Cancer Institute, 00144 Rome, Italy*
Gabriella D'Orazi − *Department of Research and Advanced Technologies, IRCCS Regina Elena, National Cancer Institute, 00144 Rome, Italy; Department of Neurosciences, Imaging and Clinical Sciences, University G. D'Annunzio, 66013 Chieti, Italy*
Agustín Galindo − *Departamento de Química Inorgánica, Facultad de Química, Universidad de Sevilla, 41012 Sevilla, Spain;* orcid.org/0000-0002-2772-9171

Complete contact information is available at: https://pubs.acs.org/10.1021/acs.jmedchem.4c01298

Author Contributions

S. Xhafa: synthesis and characterization of zinc(II) compounds. **C. Di Nicola**: formal analysis and validation. **A. Tombesi**: synthesis and characterization of ligands. **R. Pettinari**: resources and writing—review and editing. **C. Pettinari**: resources and writing—review and editing. **F. Scarpelli**: X-ray single-crystal crystallographic study. **A. Crispini**: writing—review and editing. **M. La Deda**: photophysical studies and writing—review. **A. Candreva**: X-ray single powder crystallographic study. **A. Garufi**: biological studies. **G. D'Orazi**: resources and writing—review and edition. **A. Galindo**: DFT computational study. **F. Marchetti**: funding acquisition and writing—original draft preparation.

Notes

The authors declare no competing financial interest.
The authors will release the atomic coordinates upon article publication.

■ ACKNOWLEDGMENTS

The University of Camerino is gratefully acknowledged for having financed part of S.X.'s doctoral scholarship. This work was financially supported by MUR—PNRR (Decreto Direttoriale n. 703 del 20-4-2022), within the framework of the project "VITALITY—Innovation, digitalisation and sustainability for the diffused economy in Central Italy" (cod. ECS_00000041), Spoke 9—Nanostructured materials and devices. A.G. thanks the Centro de Servicios de Informática y Redes de Comunicaciones (CSIRC), Universidad de Granada, for providing the computing time. F.S. is grateful to the project PON "Ricerca e Innovazione" 2014−2020, Asse IV "Istruzione e ricerca per il recupero", and Azione IV.6 "Contratti di ricerca su tematiche Green" (CUP: H25F21001230004; identification code: 1062_R8_GREEN).

■ ABBREVIATIONS

DFT	density functional theory
DMF	dimethylformamide
DMSO	dimethyl sulfoxide
DNA	deoxyribonucleic acid
HOMO	highest occupied molecular orbital
HSP90	Heat Shock Protein 90
IC50	half-maximum inhibitory concentration
IR	infrared
NMR	nuclear magnetic resonance
NRF2	nuclear factor erythroid 2-related factor 2
PBS	phosphate-buffered saline
PXRD	powder X-ray diffraction
R175H	mutant p53 protein
R273H	mutant p53 protein
RT-PCR	reverse transcription polymerase chain reaction
SKB3	human cancer cell line
TGA	thermogravimetric analysis
U373	human cancer cell line
UV−vis	ultraviolet−visible

■ REFERENCES

(1) Hadjoudis, E.; Mavridis, I. M. Photochromism and Thermochromism of Schiff Bases in the Solid State: Structural Aspects. *Chem. Soc. Rev.* **2004**, *33*, 579−588.
(2) Pettinari, C.; Marchetti, F.; Drozdov, A. *β*-Diketones and Related Ligands. In *Comprehensive Coordination Chemistry II*; Elsevier Ltd. All, 2003; pp 97−115.
(3) Marchetti, F.; Pettinari, C.; Pettinari, R. Acylpyrazolone Ligands: Synthesis, Structures, Metal Coordination Chemistry and Applications. *Coord. Chem. Rev.* **2005**, *249*, 2909−2945.
(4) Marchetti, F.; Pettinari, R.; Pettinari, C. Recent Advances in Acylpyrazolone Metal Complexes and Their Potential Applications. *Coord. Chem. Rev.* **2015**, *303*, 1−31.
(5) Marchetti, F.; Pettinari, C.; Di Nicola, C.; Tombesi, A.; Pettinari, R. Coordination Chemistry of Pyrazolone-Based Ligands and Applications of Their Metal Complexes. *Coord. Chem. Rev.* **2019**, *401*, 213069.
(6) Zhao, Z.; Dai, X.; Li, C.; Wang, X.; Tian, J.; Feng, Y.; Xie, J.; Ma, C.; Nie, Z.; Fan, P.; et al. Pyrazolone Structural Motif in Medicinal Chemistry: Retrospect and Prospect. *Eur. J. Med. Chem.* **2020**, *186*, 111893.
(7) Çakmak, R.; Ay, B.; Çınar, E.; Başaran, E.; Akkoç, S.; Boğa, M.; Taş, E. Synthesis, Spectroscopic, Thermal Analysis and in Vitro Cytotoxicity, Anticholinesterase and Antioxidant Activities of New Co(II), Ni(II), Cu(II), Zn(II), and Ru(III) Complexes of Pyrazolone-Based Schiff Base Ligand. *J. Mol. Struct.* **2023**, *15*, 136225−7.
(8) Başaran, E.; Çakmak, R.; Akkoç, S.; Kaya, S. Combined Experimental and Theoretical Analyses on Design, Synthesis, Characterization, and in Vitro Cytotoxic Activity Evaluation of Some Novel Imino Derivatives Containing Pyrazolone Ring. *J. Mol. Struct.* **2022**, *1265*, 133427.
(9) Çakmak, R.; Başaran, E.; Boğa, M.; Erdoğan, Ö.; Çınar, E.; Çevik, Ö. Schiff Base Derivatives of 4-Aminoantipyrine as Promising Molecules: Synthesis, Structural Characterization, and Biological Activities. *Russ. J. Bioorg. Chem.* **2022**, *48* (2), 334−344.
(10) Çınar, E.; Başaran, E.; Erdoğan, Ö.; Çakmak, R.; Boğa, M.; Çevik, Ö. Heterocyclic Schiff Base Derivatives Containing Pyrazolone Moiety: Synthesis, Characterization, and in Vitro Biological Studies. *J. Chin. Chem. Soc.* **2021**, *68* (12), 2355−2367.
(11) Shaikh, I.; Jadeja, R. N.; Patel, R.; Mevada, V.; Gupta, V. K. 4-Acylhydrazone-5-Pyrazolones and Their Zinc(II) Metal Complexes: Synthesis, Characterization, Crystal Feature and Antimalarial Activity. *J. Mol. Struct.* **2021**, *1232*, 130051.
(12) Shaikh, I. U.; Patel, R. K.; Mevada, V. A.; Gupta, V. K.; Jadeja, R. N. Binary and Ternary Zinc(II) Complexes of Acyl Pyrazolones: Synthesis, Spectroscopic Analysis, Crystal Structure and Antimalarial Activity. *ChemistrySelect* **2019**, *4*, 8286−8294.
(13) Shaikh, I.; Jadeja, R. N.; Patel, R. Three Mixed Ligand Mononuclear Zn(II) Complexes of 4-Acyl Pyrazolones: Synthesis, Characterization, Crystal Study and Anti-Malarial Activity. *Polyhedron* **2020**, *183*, 114528.

(14) Pellei, M.; Del Bello, F.; Porchia, M.; Santini, C. Zinc Coordination Complexes as Anticancer Agents. *Coord. Chem. Rev.* **2021**, *445*, 214088.
(15) D'Orazi, G.; Givol, D. P53 Reactivation: The Link to Zinc. *Cell Cycle* **2012**, *11* (14), 2581−2582.
(16) Kogan, S.; Carpizo, D. R. Zinc Metallochaperones as Mutant P53 Reactivators: A New Paradigm in Cancer Therapeutics. *Cancers* **2018**, *10* (6), 166−213.
(17) Gilleran, J. A.; Yu, X.; Blayney, A. J.; Bencivenga, A. F.; Na, B.; Augeri, D. J.; Blanden, A. R.; Kimball, S. D.; Loh, S. N.; Roberge, J. Y.; Carpizo, D. R. Benzothiazolyl and Benzoxazolyl Hydrazones Function as Zinc Metallochaperones to Reactivate Mutant P53. *J. Med. Chem.* **2021**, *64* (4), 2024−2045.
(18) Garufi, A.; Trisciuoglio, D.; Porru, M.; Leonetti, C.; Stoppacciaro, A.; D'Orazi, V.; Avantaggiati, M. L.; Crispini, A.; Pucci, D.; D'Orazi, G. A Fluorescent Curcumin-Based Zn (II)-Complex Reactivates Mutant (R175H and R273H) P53 in Cancer Cells. *J. Exp. Clin. Cancer Res.* **2013**, *32* (1), 72.
(19) Yu, X.; Kogan, S.; Chen, Y.; Tsang, A. T.; Withers, T.; Lin, H.; Gilleran, J.; Buckley, B.; Moore, D.; Bertino, J.; et al. Zinc Metallochaperones Reactivate Mutant P53 Using an ON/OFF Switch Mechanism: A New Paradigm in Cancer Therapeutics. *Clin. Cancer Res.* **2018**, *24* (18), 4505−4517.
(20) Na, B.; Yu, X.; Withers, T.; Gilleran, J.; Yao, M.; Foo, T. K.; Chen, C.; Moore, D.; Lin, Y.; Kimball, S. D.; Xia, B.; Ganesan, S.; Carpizo, D. R. Therapeutic Targeting of BRCA1 and TP53 Mutant Breast Cancer through Mutant P53 Reactivation. *npj Breast Cancer* **2019**, *5* (1), 14.
(21) Blanden, R.; Yu, X.; Aaron, J. W.; Gilleran, J. A.; Augeri, D. J.; O'Dell, R. S.; Olson, E. C.; Kimball, S. D.; Emge, T. J.; Movileanu, L.; Carpizo, D. R.; Loh, S. N. Synthetic Metallochaperone ZMC1 Rescues Mutant P53 Conformation by Transporting Zinc into Cells as an Ionophore. *Mol. Pharmacol.* **2015**, *88* (6), 1084.
(22) Puca, R.; Nardinocchi, L.; Porru, M.; Simon, A. J.; Rechavi, G.; Leonetti, C.; Givol, D.; D'Orazi, G. Restoring P53 Active Conformation by Zinc Increases the Response of Mutant P53 Tumor Cells to Anticancer Drugs. *Cell Cycle* **2011**, *10* (10), 1679−1689.
(23) Puca, R.; Nardinocchi, L.; Gal, H.; Rechavi, G.; Amariglio, N.; Domany, E.; Notterman, D. A.; Scarsella, M.; Leonetti, C.; Sacchi, A.; et al. Reversible Dysfunction of Wild-Type P53 Following Homeodomain-Interacting Protein Kinase-2 Knockdown. *Cancer Res.* **2008**, *68* (10), 3707−3714.
(24) Cirone, M.; Garufi, A.; Di Renzo, L.; Granato, M.; Faggioni, A.; D'Orazi, G. Zinc Supplementation Is Required for the Cytotoxic and Immunogenic Effects of Chemotherapy in Chemoresistant P53-Functionally Deficient Cells. *Oncoimmunology* **2013**, *2* (9), No. e26198.
(25) Garufi, A.; Ubertini, V.; Mancini, F.; D'Orazi, V.; Baldari, S.; Moretti, F.; Bossi, G.; D'Orazi, G. The Beneficial Effect of Zinc (II) on Low-Dose Chemotherapeutic Sensitivity Involves P53 Activation in Wild-Type P53-Carrying Colorectal Cancer Cells. *J. Exp. Clin. Cancer Res.* **2015**, *34* (1), 87.
(26) Kastenhuber, E. R.; Lowe, S. W. Putting P53 in Context. *Cell* **2017**, *170* (6), 1062−1078.
(27) Muller, P. A. J.; Vousden, K. H. Mutant P53 in Cancer: New Functions and Therapeutic Opportunities. *Cancer Cell* **2014**, *25* (3), 304−317.
(28) Cho, Y.; Gorina, S.; Jeffrey, P. D.; Pavletich, N. P. Crystal Structure of a P53 Tumor Suppressor-DNA Complex: Understanding Tumorigenic Mutations. *Science* **1994**, *265* (5170), 346−355.
(29) Loh, S. N. The Missing Zinc: P53 Misfolding and Cancer. *Metallomics* **2010**, *2* (7), 442−449.
(30) Méplan, C.; Richard, M.-J.; Hainaut, P. Metalloregulation of the Tumor Suppressor Protein P53: Zinc Mediates the Renaturation of P53 after Exposure to Metal Chelators in Vitro and in Intact Cells. *Oncogene* **2000**, *19* (46), 5227−5236.
(31) D'Orazi, G.; Cirone, M. Mutant P53 and Cellular Stress Pathways: A Criminal Alliance That Promotes Cancer Progression. *Cancers* **2019**, *11* (5), 614.
(32) Joerger, A.; Fersht, A. R. Structure−Function−Rescue: The Diverse Nature of Common P53 Cancer Mutants. *Oncogene* **2007**, *26* (15), 2226−2242.
(33) Muller, P. A. J.; Vousden, K. H. P53 Mutations in Cancer. *Nat. Cell Biol.* **2013**, *15* (1), 2−8.
(34) Pettinari, R.; Pettinari, C.; Marchetti, F.; Clavel, C. M.; Scopelliti, R.; Dyson, P. J. Cytotoxicity of Ruthenium−Arene Complexes Containing β-Ketoamine Ligands. *Organometallics* **2013**, *32* (1), 309−316.
(35) Pettinari, R.; Marchetti, F.; Pettinari, C.; Petrini, A.; Scopelliti, R.; Clavel, C. M.; Dyson, P. J. Synthesis, Structure, and Antiproliferative Activity of Ruthenium(II) Arene Complexes with N,O-Chelating Pyrazolone-Based β-Ketoamine Ligands. *Inorg. Chem.* **2014**, *53* (24), 13105−13111.
(36) Pettinari, R.; Marchetti, F.; Di Nicola, C.; Pettinari, C.; Galindo, A.; Petrelli, R.; Cappellacci, L.; Cuccioloni, M.; Bonfili, L.; Eleuteri, A. M.; Guedes da Silva, M. F. C.; Pombeiro, A. J. L. Ligand Design for N,O-or N,N-Pyrazolone-Based Hydrazones Ruthenium-(II)-Arene Complexes and Investigation of Their Anticancer Activity. *Inorg. Chem.* **2018**, *57*, 14123−14133.
(37) Cuccioloni, M.; Bonfili, L.; Cecarini, V.; Nabissi, M.; Pettinari, R.; Marchetti, F.; Petrelli, R.; Cappellacci, L.; Angeletti, M.; Eleuteri, A. M. Exploring the Molecular Mechanisms Underlying the in Vitro Anticancer Effects of Multitarget-Directed Hydrazone Ruthenium (II)−Arene Complexes. *ChemMedChem* **2020**, *15* (1), 105−113.
(38) Gusev, A.; Braga, E.; Tyutyunik, A.; Gurchenko, V.; Berezovskaya, M.; Kryukova, M.; Kiskin, M.; Linert, W. Synthesis, Photoluminescence and Electrical Study of Pyrazolone-Based Azomethine Ligand Zn(II) Complexes. *Materials* **2020**, *13*, 5698.
(39) Yang, L.; Powell, D. R.; Houser, R. P. Structural Variation in Copper (I) Complexes with Pyridylmethylamide Ligands: Structural Analysis with a New Four-Coordinate Geometry Index, τ 4. *Dalton Trans.* **2007**, No. 9, 955−964.
(40) Gusev, A.; Braga, E.; Tyutyunik, A.; Gurchenko, V.; Berezovskaya, M.; Kryukova, M.; Kiskin, M.; Linert, W. Synthesis, Photoluminescence and Electrical Study of Pyrazolone-Based Azomethine Ligand Zn(Ii) Complexes. *Materials* **2020**, *13* (24), 5698.
(41) Vinci, M.; Gowan, S.; Boxall, F.; Patterson, L.; Zimmermann, M.; Court, W.; Lomas, C.; Mendiola, M.; Hardisson, D.; Eccles, S. A. Advances in establishment and analysis of three-dimensional tumor spheroid-based functional assays for target validation and drug evaluation. *BMC Biol.* **2012**, *10* (1), 29.
(42) Lee, K. H.; Kim, T. H. Recent Advances in Multicellular Tumor Spheroid Generation for Drug Screening. *Biosensors* **2021**, *11* (11), 445.
(43) Costa, E. C.; Moreira, A. F.; de Melo-Diogo, D.; Gaspar, V. M.; Carvalho, M. P.; Correia, I. J. 3D Tumor Spheroids: An Overview on the Tools and Techniques Used for Their Analysis. *Biotechnol. Adv.* **2016**, *34* (8), 1427−1441.
(44) Garufi, A.; Pucci, D.; D'Orazi, V.; Cirone, M.; Bossi, G.; Avantaggiati, M. L.; D'Orazi, G. Degradation of Mutant P53H175 Protein by Zn(II) through Autophagy. *Cell Death Dis.* **2014**, *5* (5), e1271−e1279.
(45) Gilardini Montani, M. S.; Cecere, N.; Granato, M.; Romeo, M. A.; Falcinelli, L.; Ciciarelli, U.; D'orazi, G.; Faggioni, A.; Cirone, M. Mutant p53, Stabilized by Its Interplay with HSP90, Activates a Positive Feed-Back Loop Between NRF2 and p62 that Induces Chemo-Resistance to Apigenin in Pancreatic Cancer Cells. *Cancers* **2019**, *11* (5), 703.
(46) Garufi, A.; Giorno, E.; Gilardini Montani, M. S.; Pistritto, G.; Crispini, A.; Cirone, M.; D'orazi, G. P62/Sqstm1/Keap1/Nrf2 Axis Reduces Cancer Cells Death-Sensitivity in Response to Zn(Ii)−Curcumin Complex. *Biomolecules* **2021**, *11* (3), 348−412.
(47) Garufi, A.; Pistritto, G.; D'orazi, V.; Cirone, M.; D'orazi, G. The Impact of NRF2 Inhibition on Drug-Induced Colon Cancer Cell

Death and P53 Activity: A Pilot Study. *Biomolecules* **2022**, *12* (3), 461−513.
(48) Marchetti, F.; Tombesi, A.; Di Nicola, C.; Pettinari, R.; Verdicchio, F.; Crispini, A.; Scarpelli, F.; Baldassarri, C.; Marangoni, E.; Hofer, A.; et al. Zinc (II) Complex with Pyrazolone-Based Hydrazones Is Strongly Effective against Trypanosoma Brucei Which Causes African Sleeping Sickness. *Inorg. Chem.* **2022**, *61* (34), 13561−13575.
(49) Alfadul, S. M.; Matnurov, E. M.; Varakutin, A. E.; Babak, M. V. Metal-Based Anticancer Complexes and P53: How Much Do We Know? *Cancers* **2023**, *15* (10), 2834.
(50) Profex Open Source XRD and Rietveld Refinement. https://www.profex-xrd.org (accessed June 22, 2024).
(51) SAINT. Bruker AXS Inc: Madison, WI, USA, 2003.
(52) Sheldrick, G. M. *SADABS Empirical Absorption Program*; Madison: WI, USA, 2003.
(53) Krause, L.; Herbst-Irmer, R.; Sheldrick, G. M.; Stalke, D. Comparison of Silver and Molybdenum Microfocus X-Ray Sources for Single-Crystal Structure Determination. *J. Appl. Crystallogr.* **2015**, *48*, 3−10.
(54) Sheldrick, G. M. A. A short history of SHELX. *Acta Crystallogr., Sect. A: Found. Crystallogr.* **2008**, *64* (1), 112−122.
(55) Sheldrick, G. M. Crystal Structure Refinement with SHELXL. *Acta Crystallogr., Sect. C: Struct. Chem.* **2015**, *71*, 3−8.
(56) Müller, P. Practical Suggestions for Better Crystal Structures. *Crystallogr. Rev.* **2009**, *15* (1), 57−83.
(57) Garufi, A.; Baldari, S.; Pettinari, R.; Gilardini Montani, M. S.; D'Orazi, V.; Pistritto, G.; Crispini, A.; Giorno, E.; Toietta, G.; Marchetti, F.; et al. A Ruthenium (II)-Curcumin Compound Modulates NRF2 Expression Balancing the Cancer Cell Death/Survival Outcome According to P53 Status. *J. Exp. Clin. Cancer Res.* **2020**, *39* (1), 122−215.
(58) Becke, A. D. Density-functional Thermochemistry. III. The Role of Exact Exchange. *J. Chem. Phys.* **1993**, *98* (7), 5648−5652.
(59) Lee, C.; Yang, W.; Parr, R. G. Development of the Colle-Salvetti Correlation-Energy Formula into a Functional of the Electron Density. *Phys. Rev. B* **1988**, *37* (2), 785−789.
(60) Wong, M. W. Vibrational Frequency Prediction Using Density Functional Theory. *Chem. Phys. Lett.* **1996**, *256* (4−5), 391−399.
(61) Scott, A. P.; Radom, L. Harmonic Vibrational Frequencies: An Evaluation of Hartree− Fock, Møller− Plesset, Quadratic Configuration Interaction, Density Functional Theory, and Semiempirical Scale Factors. *J. Phys. Chem.* **1996**, *100* (41), 16502−16513.
(62) Frisch, M. J.; Trucks, G. W.; Schlegel, H. B.; Scuseria, G. E.; Robb, M. A.; Cheeseman, J. R.; Scalmani, G.; Barone, V.; Petersson, G. A.; Nakatsuji, H.; Li, X.; Caricato, M.; Marenich, A. V.; Bloino, J.; Janesko, B. G.; Gomperts, R.; Mennucci, B.; Hratchian, H. P.; et al. *Gaussian 16*, Revision B.01, Gaussian Inc: Wallingford CT, 2016.

https://doi.org/10.1021/acs.jmedchem.4c01298
J. Med. Chem. 2024, 67, 15676−15690